Large magnetoresistance in the type-II Weyl semimetal semimetal WP[subscript 2]

PHYSICAL REVIEW B **96**, 121107(R) (2017)

Large magnetoresistance in the type-II Weyl semimetal WP_2

Aifeng Wang (王爱峰),[1] D. Graf,[2] Yu Liu (刘育),[1] Qianheng Du (杜乾衡),[1,3] Jiabao Zheng (郑佳宝),[4,5] Hechang Lei (雷和畅),[6] and C. Petrovic[1,3]

[1]*Condensed Matter Physics and Materials Science Department, Brookhaven National Laboratory, Upton, New York 11973, USA*

[2]*National High Magnetic Field Laboratory, Florida State University, Tallahassee, Florida 32306-4005, USA*

[3]*Department of Materials Science and Chemical Engineering, Stony Brook University, Stony Brook, New York 11790, USA*

[4]*Department of Electrical Engineering, Columbia University, New York, New York 10027, USA*

[5]*Department of Electrical Engineering and Computer Science, Massachusetts Institute of Technology, Cambridge, Massachusetts 02139, USA*

[6]*Department of Physics and Beijing Key Laboratory of Opto-electronic Functional Materials and Micro-nano Devices, Renmin University of China, Beijing 100872, People's Republic of China*

(Received 25 April 2017; published 11 September 2017; corrected 25 September 2017)

We report a magnetotransport study on type-II Weyl semimetal WP_2 single crystals. Magnetoresistance exhibits a nonsaturating H^n field dependence (14 300% at 2 K and 9 T), whereas systematic violation of Kohler's rule was observed. Quantum oscillations reveal a complex multiband electronic structure. The cyclotron effective mass close to the mass of free electron m_e was observed in quantum oscillations along the b axis, while a reduced effective mass of about $0.5m_e$ was observed in a-axis quantum oscillations, suggesting Fermi surface anisotropy. The temperature dependence of the resistivity shows a large upturn that cannot be explained by the multiband magnetoresistance of conventional metals. Even though the crystal structure of WP_2 is not layered as in transition-metal dichalcogenides, quantum oscillations suggest partial two-dimensional character.

DOI: 10.1103/PhysRevB.96.121107

I. INTRODUCTION

Weyl fermions originate from Dirac states by breaking either time-reversal symmetry or space-inversion symmetry [1–12]. In addition to type-I [3,6,10] Weyl points with a close pointlike Fermi surface, novel type-II [4,11] Weyl fermions appear at the boundaries between electron and hole pockets violating Lorentz invariance. This results in an open Fermi surface and anisotropic chiral anomaly. Most of the reported type-II Weyl semimetals exhibit characteristic extraordinary magnetoresistance (XMR), observed, for example, in materials that crystallize in the $C2/m$ space group of $OsGe_2$-type structure, such as $NbSb_2$, $TaAs_2$, and $NbAs_2$ [13,14].

WP_2 crystallizes the nonsymmorphic space group $Cmc2_1(36)$, which favors new topological phases with Dirac states [15–18]. Indeed, WP_2 was recently predicted to be a type-II Weyl semimetal with four pairs of type-II Weyl points and long topological Fermi arcs [19]. In this work, we have successfully grown single crystals of WP_2, and have investigated its magnetotransport properties. Magnetoresistance ($MR = [\rho(B) - \rho(0)]/\rho(0) \times 100\%$) exhibits a nonsaturating $\sim H^{1.8}$ field dependence up to 14 300% at 2 K and 9 T. WP_2 shows a systematic violation of Kohler's rule and large magnetic-field-induced nonmetallic resistivity that cannot be explained by orbital magnetoresistance of multiband metals. Fermi surface studies of WP_2 by quantum oscillations reveal a complex electronic structure. The T-H phase diagram is consistent with the universal phase diagram for XMR materials [20]. However, the Weyl points in WP_2 have little influence on the effective mass and mobility of the Fermi surfaces detected by quantum oscillations.

II. EXPERIMENTAL DETAILS

Single crystals of WP_2 were grown by chemical vapor transport method using I_2 as the transport agent. First, WP_2 polycrystals were obtained by annealing stoichiometric W and P powder at 500 °C for 24 h, and then 750 °C for 48 h. WP_2 polycrystals were mixed with I_2 (15 mg/ml), and then sealed in an evacuated quartz tube. Single crystals were grown in a temperature gradient 1180 °C (source) to 1050 °C (sink) for a month. Shiny needlelike single crystals with typical size 1.5 mm × 0.05 mm × 0.05 mm were obtained. X-ray diffraction measurements were performed using a Rigaku Miniflex powder diffractometer. The element analysis was performed using an energy-dispersive x-ray spectroscopy (EDX) in a JEOL LSM 6500 scanning electron microscope. Heat capacity and magnetotransport measurements up to 9 T were conducted in a Quantum Design PPMS-9. Magnetotransport measurements at high magnetic fields up to 18 T were conducted at the National High Magnetic Field Laboratory in Tallahassee. Resistivity was measured using a standard four-probe configuration. Hall resistivity was measured by the four-terminal technique by switching the polarity of the magnetic field to eliminate the contribution of ρ_{xx} due to the misalignment of the voltage contacts.

III. RESULTS AND DISCUSSIONS

Figure 1(a) shows the powder x-ray diffraction pattern of WP_2. The data can be fitted quite well by the space group $Cmc2_1$ with lattice parameter $a = 0.3164(2)$ nm, $b = 1.184(2)$ nm, and $c = 0.4980(2)$ nm, consistent with a previous report [15]. The average atomic ratio determined by the EDX is W : P = 1:2. Figure 1(b) shows the temperature dependence of resistivity in WP_2 in different fields. The residual resistivity ratio (RRR) in the absence of magnetic field is $\rho(300\ \mathrm{K})/\rho(2\ \mathrm{K}) = 279$ with $\rho(2\ \mathrm{K}) = 0.19\ \mu\Omega\,\mathrm{cm}$, indicating small defect scattering in the crystal. The metallic resistivity in $H = 0$ can be described by the Bloch-Grüneisen (BG) model [21]:

$$\rho(T) = \rho_0 + C\left(\frac{T}{\Theta_D}\right)^5 \int_0^{\Theta_D/T} \frac{x^5}{(e^x - 1)(1 - e^{-x})} dx,$$

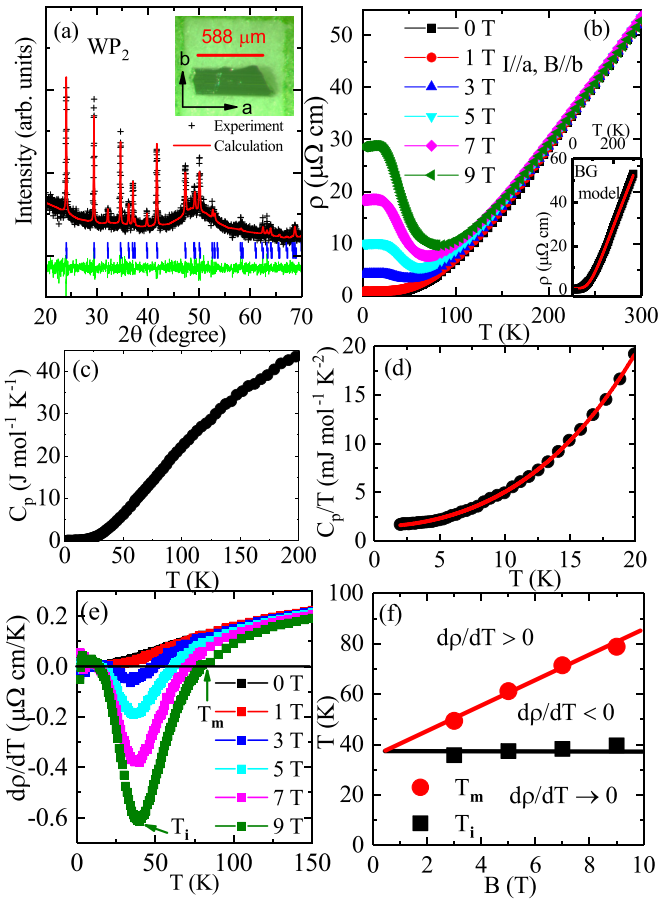

FIG. 1. (a) Powder x-ray diffraction pattern of WP_2, inset shows a photograph of as-grown single crystal. (b) Temperature-dependent transversal resistivity for WP_2 in different magnetic fields. Inset shows $\rho(0\ \mathrm{T})$ fitted with the Bloch-Grüneisen model. Heat capacity of WP_2 [(c),(d)]. The $(\partial\rho/\partial T)$ plotted as a function of temperature (e); minima and sign change points in the $\partial\rho/\partial T$ are defined as T_m and T_i, respectively. Magnetic field dependence of T_m and T_i (f).

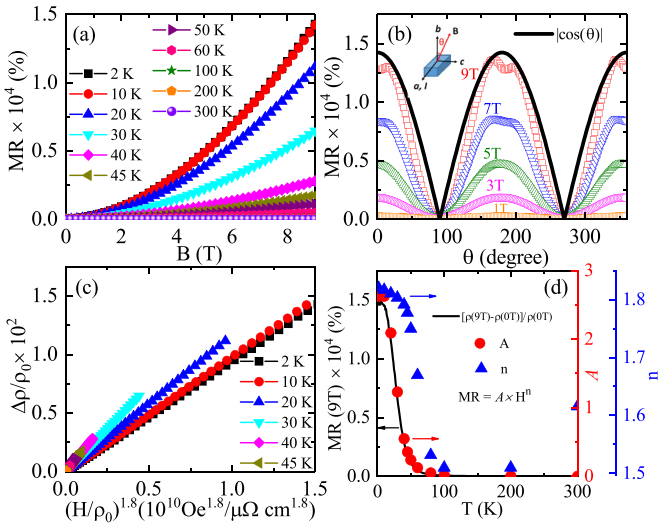

FIG. 2. Magnetic-field dependence of MR at various temperatures (a) and magnetoresistance as a function of the tilted angle from the applied field (b). Black line is the fitting using the 2D model. Kohler plot at different temperatures using $\Delta\rho/\rho(0) = F[H/\rho(0)] \simeq H^{1.8}$ (c). MR versus temperature for WP_2 at 9 T (left) and temperature dependence of A and n ($\mathrm{MR} = A \times H^n$) (right) (d).

where ρ_0 is the residual resistivity and Θ_D is the Debye temperature, indicating phonon scattering in the whole temperature range. The fitting results in $\Theta_D = 546(5)$ K. As shown in Fig. 1(b), with the application of the magnetic field, the $\rho(T)$ shows a large upturn which saturates below ~15 K. Similar resistivity behavior was observed recently in XMR materials such as WTe_2, TaAs, LaSb, $PtSn_4$, ZrSiSe, and Ta_3S_2, but also in graphite, bismuth, and MgB_2 [22–31]. The heat capacity of WP_2, shown in Fig. 1(c), is best described at low temperatures with a $C(T)/T = \gamma + \beta T^2 + \delta T^4$ where $\gamma = 1.50(5)\ \mathrm{mJ\ mol^{-1}\ K^{-1}}$, $\beta = 0.0324(5)\ \mathrm{mJ\ mol^{-1}\ K^{-2}}$, and $\delta = 3.0(2) \times 10^{-5}\ \mathrm{mJ\ mol^{-1}\ K^{-4}}$ [Fig. 1(d)] [32]. The Debye temperature $\Theta_D = 564(\pm 11)$ K is obtained from $\Theta_D = (12\pi^4 NR/5\beta)^{1/3}$ where N is the atomic number in the chemical formula and R is the gas constant.

Based on the field dependence of $\partial\rho/\partial T$ [Fig. 1(e)] we plot the temperature-field (T-H) phase diagram in Fig. 1(f), where T_m and T_i are taken as the sign change point and minimum in $\partial\rho/\partial T$. The phase diagram is consistent with extreme magnetoresistance materials [20].

Figure 2(a) shows the field dependence of transverse magnetoresistance $\mathrm{MR} = [\rho(B) - \rho(0)]/\rho(0) \times 100\%$ at various temperatures with $B \| b$. MR exhibits a nonsaturating $\sim H^{1.8}$ dependence and reaches 14 300% at 2 K and 9 T. It decreases quickly with increasing temperature, and becomes negligibly small above 100 K. The MR of WP_2 is about one order of magnitude smaller than in WTe_2 and LaSb, but comparable even larger than those in LaBi, Ta_3S_2, and $TaIrTe_4$ [22–25,33]. The MR of solids only responds to the extremal cross section of the Fermi surface along the field direction. Thus, angular dependence of MR in a material with a two-dimensional (2D) Fermi surface should be proportional to $|\cos(\theta)|$ [34]. As shown in Fig. 2(b), MR in different magnetic fields shows twofold symmetry which can be fitted well with $|\cos(\theta)|$, indicating a 2D Fermi surface.

Field-induced nonmetallic resistivity and XMR in topological materials has been discussed lately in the literature; however, its origin was ascribed to different mechanisms. In WTe_2 it was suggested that the band structure of a compensated semimetal with perfect electron-hole symmetry is important, whereas in LaBi and LaSb the proposed mechanism involves a combination of compensated electron-hole pockets and particular orbital texture on the electron pocket [20,35–38]. There is also evidence for exotic and multiple surface Dirac states in other materials. MR in $PtSn_4$ has been considered within the model of orbital MR in the long mean-free-path metals with single dominant scattering time [28]. However, Dirac node arcs are also found in $PtSn_4$ and ZrSiSe(Te), suggesting that XMR could be connected with suppressed backscattering of Dirac states [39,40].

Semiclassical transport theory based on the Boltzmann equation predicts Kohler's rule $\Delta\rho/\rho(0) = F[H/\rho(0)]$ to hold if there is a single type of charge carrier and scattering time in a metal [41]. Violation of Kohler's rule is common in XMR materials, such as LaBi, TaAs, $TaAs_2$, $NbAs_2$, and $NbSb_2$ [13,14,23,42]. As shown in Fig. 2(c), MR in WP_2 systematically deviates from Kohler's rule above 10 K. The

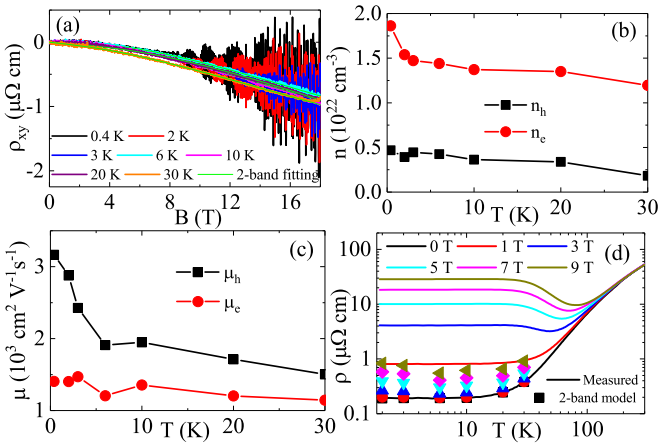

FIG. 3. (a) The magnetic field dependence of Hall resistivity ρ_{xy} at various temperatures. The temperature dependence of carrier densities (b) and mobilities (c) of electrons and holes obtained by fitting using the two-band model. (d) Measured temperature dependence of $\rho(T,B)$ at various fields (solid lines), and $\rho(T,B)$ calculated using the temperature dependence of $n_{e,h}$ and $\mu_{e,h}$ derived from the two-band model (scatter symbols).

field dependence of MR at different temperatures can be well fitted with $\mathrm{MR} = A \times H^n$; n is 1.8 at 2 K. The exponent n systematically decreases to 1.5 with increasing temperature, as shown in Fig. 2(d). The temperature evolutions of A and n are similar to the temperature dependence of MR(9 T).

A common violation of Kohler's rule in metals is multiband electronic transport, i.e., the existence of multiple scattering times. WP_2 was predicted to be a type-II Weyl semimetal; therefore there is a possibility that high mobility bands with Dirac states contribute to small residual resistivity in zero magnetic field and strong magnetoresistance. In the two-band model MR is [43]

$$\mathrm{MR} = \frac{n_e\mu_e n_h\mu_h(\mu_e+\mu_h)^2(\mu_0 H)^2}{(\mu_e n_h+\mu_h n_e)^2+(\mu_h\mu_e)^2(\mu_0 H)^2(n_h-n_e)^2}.$$

For the compensated semimetal, where $n_e \simeq n_h$, we obtain $MR = \mu_e\mu_h(\mu_0 H)^2$, since the $\mathrm{MR} = A \times H^n$ ($n = 1.5$–1.8) [Fig. 2(c)] compensated two-band model cannot completely explain the MR. Next, we discuss electronic transport in WP_2 from the perspective of the two-band model when $n_e \neq n_h$.

Figure 3(a) shows the field dependence of Hall resistivity ρ_{xy} at different temperatures. Clear quantum oscillations were observed at low temperatures. The frequencies and effective mass derived from ρ_{xy} are consistent with that of ρ_{xx}, and we discuss this below. The ρ_{xy} can be fitted by the two-band model:

$$\frac{\rho_{xy}}{\mu_0 H} = R_H = \frac{1}{e}\frac{(\mu_h^2 n_h-\mu_e^2 n_e)+(\mu_h\mu_e)^2(\mu_0 H)^2(n_h-n_e)}{(\mu_e n_h+\mu_h n_e)^2+(\mu_h\mu_e)^2(\mu_0 H)^2(n_h-n_e)^2},$$

where n_e (n_h) and μ_e (μ_h) denote the carrier concentrations and mobilities of electrons and holes, respectively. We find that ρ_{xy} can be well fitted by the two-band model. The obtained n_e (n_h) and μ_e (μ_h) by fitting are shown in Figs. 3(b) and 3(c), respectively. WP_2 shows relatively high carrier density and the dominant carrier is electronlike. The mobility is similar to other Dirac materials such as $A\mathrm{MnBi}_2$ (A = Sr, Ca), LaBi, and doped WTe_2 [23,44–46]. The large carrier density indicates that WP_2 is different from a compensated semimetal. We calculate the $\rho(T,B)$ using carrier concentrations n_e (n_h) and mobilities μ_e (μ_h) obtained by a two-band model fitting of ρ_{xy}, as shown in Fig. 3(d). A similar temperature dependence between calculated and measured MR argues in favor of the validity of multicarrier electronic transport [Fig. 3(d)]. However, in contrast to LaBi, the $\rho(T,B)$ from two-band orbital magnetoresistance is several orders of magnitude smaller than the measured $\rho(T,B)$. When considering the multiband behavior, further fits of ρ_{xy} using a three-band model [47] reproduced ρ_{xy} equally well. Moreover, nearly identical MR is obtained. Therefore, in either case multiband MR is much smaller than experiment results. This suggests possible contribution beyond the conventional orbital magnetoresistance that amplifies MR.

MR for $H \| b$, and cantilver for $H \| a$ at different temperatures up to 18 T are shown in Figs. 4(a) and 4(b). MR shows nonsaturating H^n up to 18 T, consistent with the results in Fig. 2. Clear oscillations were observed above 10 T. The oscillatory components are plotted as a function of $1/B$ in Figs. 4(c) and 4(d). Both Figs. 4(c) and 4(d) exhibit beat patterns, indicating that multiple frequencies contribute to oscillations. The fast Fourier transform (FFT) spectra of the oscillatory components are shown in Figs. 4(e) and 4(f). Four frequencies are observed in Fig. 4(e): 1384, 1799, 3183, and 3806 T. There are several peaks around $F_\alpha = 1384$ T, suggesting the contribution of several extrema. According to the calculated Fermi surface of WP_2 [19,48], $F_\alpha = 1384$ T and $F_\beta = 1799$ T can be ascribed to hole pockets, and $F_\gamma = 3183$ T and $F_\eta = 3806$ T are from electron pockets.

From the Onsager relation, $F = (\Phi_0/2\pi^2)A_F$, where Φ_0 is the flux quantum and A_F is the orthogonal cross-sectional area of the Fermi surface, the Fermi surface is estimated to be 13, 17, 30, and 36 nm^{-2}, corresponding to 5%, 7%, 12%, and 14% of the total area of the Brillouin zone in the ac plane. Assuming the circular cross section of Fermi surface $A_F = \pi k_F^2$, the band splitting induced by spin-orbital coupling can be estimated to be $k_\gamma - k_\eta = 0.03$ Å^{-1}, which is larger than that in MoP, and about half of that in giant Rashba effect material BiTeI [49,50]. Strong spin-orbital coupling in WP_2 indicates that spin texture, which could forbid backscattering, might play an important role in large magnetoresistance, similar to that in WTe_2 [51]. For de Haas–van Alphen (dHvA) oscillation along the a axis, the Fermi surfaces from three frequencies 1217, 2949, and 3417 T are 12, 28, and 32, corresponding to 18%, 42%, and 48% of the Brillouin zone.

In order to obtain the cyclotron mass for the main frequencies, the FFT amplitude A versus temperature was fitted using the Lifshitz-Kosevich formula [34], $A \sim [\alpha m^*(T/B)/\sinh(\alpha m^* T/B)]$ where $\alpha = 2\pi^2 k_B/e\hbar \approx 14.69$ T/K and $m^* = m/m_e$ is the cyclotron mass ratio (m_e is the mass of free electron). As shown in Figs. 4(e) and 4(f), the cyclotron mass along the b axis is close to the mass of free electron m_e, while the cyclotron mass along the a axis is reduced to about $0.5m_e$, which can be attributed to anisotropy of the Fermi surface. We estimate the Dingle temperatures from the FFT frequency with highest FFT peaks to be 2.4 and 4.7 K for $H \| b$ and $H \| a$, respectively. The corresponding

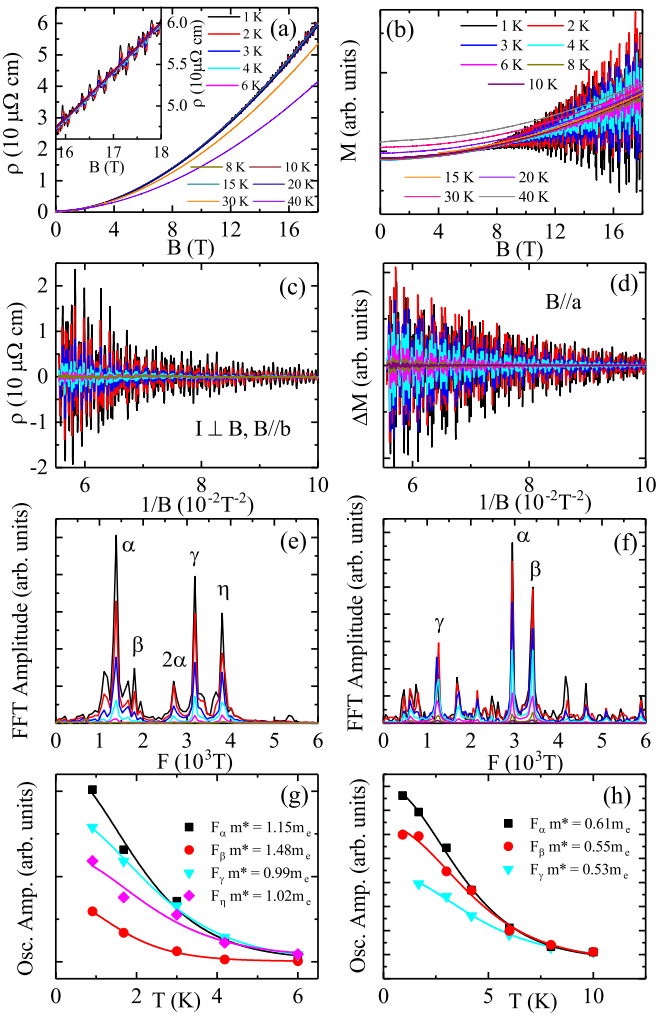

FIG. 4. Transverse resistivity vs field ($B\|b$) at different temperatures (a); inset shows the enlarged part in high magnetic field. Magnetization ($B\|a$) measured up to 18 T at various temperatures (b). SdH (c) and dHvA (d) oscillatory components obtained by smooth background subtraction. FFT spectra for SdH (e)and dHvA (f), respectively. Temperature dependence of oscillating amplitude at different frequencies for SdH (g) and dHvA (h), respectively, Solid lines are fitted using the Lifshitz-Kosevich formula.

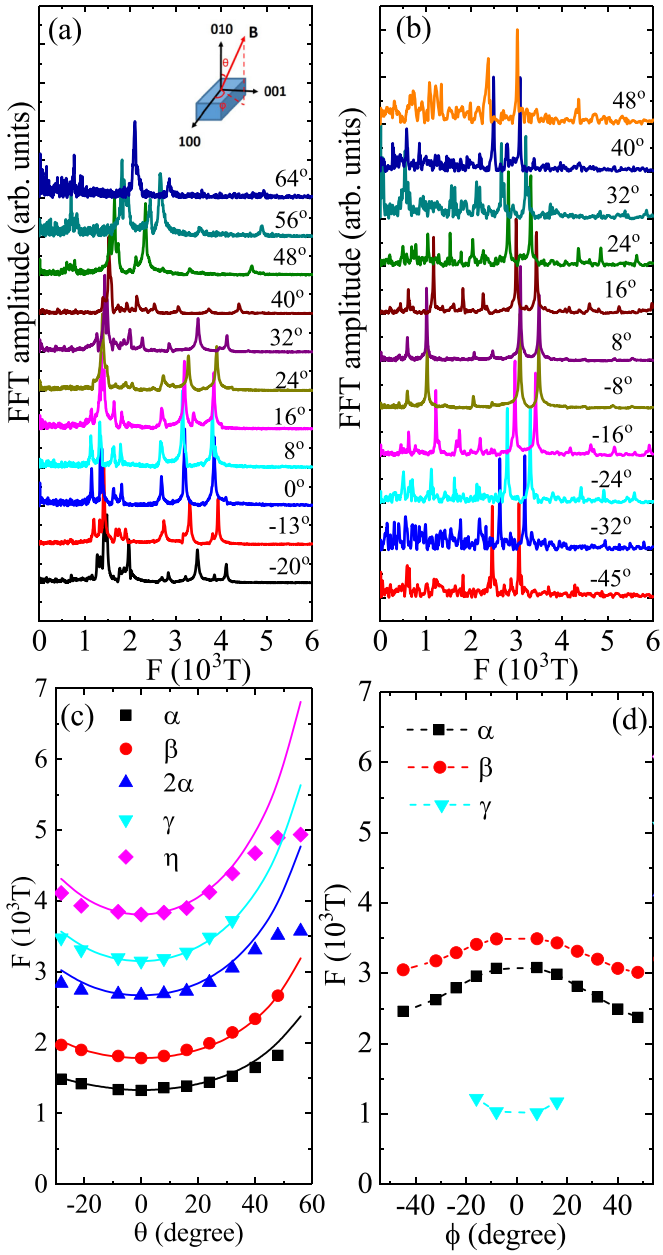

FIG. 5. FFT spectra of the SdH oscillation with field rotated in the bc plane (a) and FFT spectra of the dHvA with field rotated in the ac plane (b). Angular dependence of the oscillation frequency for SdH (c) and dHvA (d). The spectra are normalized and shifted vertically for clarity; solid lines are fitted with the 2D model $1/\cos(\theta)$.

scattering times are 5.0×10^{-13} s and 2.6×10^{-13} s. Then, the mobility estimated by $\mu_q = e\tau_q/m_c$ is 880 $\mathrm{cm^2\,V^{-1}\,s^{-1}}$ and 458 $\mathrm{cm^2\,V^{-1}\,s^{-1}}$, comparable to Fig. 3(c). The effective mass and mobility suggest that the Fermi surfaces detected by quantum oscillation are not under significant influence of the Weyl points which are located below the Fermi level [19].

The angle dependence of Shubnikov–de Haas (SdH) in the bc plane, and dHvA in the ac plane provides further insight into the shape of the Fermi surface. The FFT spectra of the SdH is presented in Fig. 5(a), and dHvA in Fig. 5(b). For the SdH measurement, four main peaks are observed; the FFT peaks increase with the angle tilt from zero, and disappear above 60°. The solid lines in Fig. 5(c) are fitted using the 2D Fermi surface [$F(0)/\cos(\theta)$]. Hence low angle quantum oscillations reveal quasi-2D character at low angles below 50°. When the field is rotated in the ac plane, with the field titled from the a axis, the frequency decreases with the angle, indicating the elongated Fermi surface in the bc plane. The angle dependence of quantum oscillations agree well with the calculated Fermi surface [19,48]. The calculated Fermi surfaces of WP_2 consist of spaghetti-like hole Fermi surfaces and bow-tie-like electron Fermi surfaces, while the presence of strong spin-orbit coupling leads to splitting of Fermi surfaces [19,48]. The spaghetti-like hole Fermi surface extends along the b axis, bends along the a axis, while it is flat along the c axis, consistent with the quasi-2D elongated α and β bands in the bc plane. When a magnetic field is applied in small angles around the b axis, SdH oscillations of γ and η bands are from

the orbits across whole electron pockets in the ac plane, and the quasi-2D behavior of γ and η bands can then be attributed to the relatively flat wall of electron pockets. Moreover, the appearance in pairs of both the hole and electron Fermi surfaces with almost the same angle dependence might be the result of the band splitting effect which is induced by strong spin-orbit coupling.

IV. CONCLUSIONS

In conclusion, magnetotransport studies of WP_2 confirm the presence of multiple bands [19]. The large increase of resistivity in magnetic field cannot be explained by the multiband orbital magnetoresistance but the effective mass and mobility detected by quantum oscillations are not under significant influence of Weyl points. A strong spin-orbit coupling effect was observed in quantum oscillations, whereas the temperature and angle dependence of quantum oscillation measurements reveal anisotropic multiband characteristics and are in agreement with calculations. Even though the crystal structure in WP_2 is not layered as in transition-metal dichalcogenides, Fermi surfaces do show partial quasi-2D character.

Note added. Recently, a related study on WP_2 was reported by Schönemann *et al.* [52]; although the magnitude of magnetoresistance and RRR of the crystal is somewhat different, the Fermi surface and main conclusion are consistent with ours.

ACKNOWLEDGMENTS

We thank John Warren for help with EDX measurements and Rongwei Hu for useful discussions. Work at BNL was supported by the U.S. DOE-BES, Division of Materials Science and Engineering, under Contract No. DE-SC0012704. Work at the National High Magnetic Field Laboratory is supported by the NSF Cooperative Agreement No. DMR-1157490, and by the state of Florida.

[1] T. O. Wehling, A. M. Black-Schaffer, and A. V. Balatsky, Adv. Phys. **63**, 1 (2014).
[2] X. Wan, A. M. Turner, A. Vishwanath, and S. Y. Savrasov, Phys. Rev. B **83**, 205101 (2011).
[3] L. Balents, Physics **4**, 36 (2011).
[4] A. A. Soluyanov, D. Gresch, Z. Wang, Q. Wu, M. Troyer, X. Dai, and B. A. Bernevig, Nature (London) **527**, 495 (2015).
[5] O. Vafek and A. Vishwanath, Annu. Rev. Condens. Matter Phys. **5**, 83 (2014).
[6] A. Bansil, H. Lin, and T. Das, Rev. Mod. Phys. **88**, 021004 (2016).
[7] M. Z. Hasan and C. L. Kane, Rev. Mod. Phys. **82**, 3045 (2010).
[8] S. Jia, S.-Y. Xu, and M. Z. Hasan, Nat. Mater. **15**, 1140 (2016).
[9] A. A. Burkov, Nat. Mater. **15**, 1145 (2016).
[10] J. Liu and D. Vanderbilt, Phys. Rev. B **90**, 155316 (2014).
[11] H. Zheng, G. Bian, G. Chang, H. Lu, S.-Y. Xu, G. Wang, T.-R. Chang, S. Zhang, I. Belopolski, N. Alidoust, D. S. Sanchez, F. Song, H.-T. Jeng, N. Yao, A. Bansil, S. Jia, H. Lin, and M. Z. Hasan, Phys. Rev. Lett. **117**, 266804 (2016).
[12] X. Dai, Nat. Mater. **15**, 5 (2015).
[13] K. Wang, D. Graf, L. Li, L. Wang, and C. Petrovic, Sci. Rep. **4**, 7328 (2014).
[14] Z. Yuan, H. Lu, Y. Liu, J. Wang, and S. Jia, Phys. Rev. B **93**, 184405 (2016).
[15] S. Rundqvist and T. Lundstrom, Acta Chem. Scand. **17**, 37 (1963).
[16] S. M. Young and C. L. Kane, Phys. Rev. Lett. **115**, 126803 (2015).
[17] T. Bzdušek, Q. Wu, A. Rüegg, M. Sigrist, and A. A. Soluyanov, Nature (London) **538**, 75 (2016).
[18] Y. X. Zhao and A. P. Schnyder, Phys. Rev. B **94**, 195109 (2016).
[19] G. Autes, D. Gresch, M. Troyer, A. A. Soluyanov, and O. V. Yazyev, Phys. Rev. Lett. **117**, 066402 (2016).
[20] F. F. Tafti, Q. Gibson, S. Kushwaha, J. W. Krizan, N. Haldolaarachchige, and R. J. Cava, Proc. Natl. Acad. Sci. USA **113**, E3475 (2016).
[21] M. Ziman, *Electrons and Phonons* (Clarendon Press, Oxford, 1962).
[22] F. F. Tafti, Q. D. Gibson, S. K. Kushwaha, N. Haldolaarachchige, and R. J. Cava, Nat. Phys. **12**, 272 (2015).
[23] S. Sun, Q. Wang, P.-J. Guo, K. Liu, and H. Lei, New J. Phys. **18**, 082002 (2016).
[24] M. N. Ali, J. Xiong, S. Flynn, J. Tao, Q. D. Gibson, L. M. Schoop, T. Liang, N. Haldolaarachchige, M. Hirschberger, N. P. Ong, and R. J. Cava, Nature (London) **514**, 205 (2014).
[25] D. Chen, L. X. Zhao, J. B. He, H. Liang, S. Zhang, C. H. Li, L. Shan, S. C. Wang, Z. A. Ren, C. Ren, and G. F. Chen, Phys. Rev. B **94**, 174411 (2016).
[26] X. Huang, L. Zhao, Y. Long, P. Wang, D. Chen, Z. Yang, H. Liang, M. Xue, H. Weng, Z. Fang, X. Dai, and G. Chen, Phys. Rev. X **5**, 031023 (2015).
[27] M. M. Hosen, K. Dimitri, I. Belopolski, P. Maldonado, R. Sankar, N. Dhakal, G. Dhakal, T. Cole, P. M. Oppeneer, D. Kaczorowski, F. Chou, M. Z. Hasan, T. Durakiewicz, and M. Neupane, Phys. Rev. B **95**, 161101(R) (2017).
[28] E. Mun, H. Ko, G. J. Miller, G. D. Samolyuk, S. L. Bud'ko, and P. C. Canfield, Phys. Rev. B **85**, 035135 (2012).
[29] D. E. Soule, Phys. Rev. **112**, 698 (1958).
[30] Z. Zhu, A. Collaudin, B. Fauqué, W. Kang, and K. Behnia, Nat. Phys. **8**, 89 (2011).
[31] S. L. Bud'ko, C. Petrovic, G. Lapertot, C. E. Cunningham, P. C. Canfield, M.-H. Jung, and A. H. Lacerda, Phys. Rev. B **63**, 220503 (2001).
[32] A. Cezairliyan, *Specific Heat of Solids* (Hemisphere Pub. Corp., New York, 1988).
[33] S. Khim, K. Koepernik, D. V. Efremov, J. Klotz, T. Förster, J. Wosnitza, M. I. Sturza, S. Wurmehl, C. Hess, J. van den Brink, and B. Büchner, Phys. Rev. B **94**, 165145 (2016).
[34] D. Shoeneberg, *Magnetic Oscillation in Metals* (Cambridge University Press, Cambridge, 1984).
[35] L. Wang, I. Gutierrez-Lezama, C. Barreteau, N. Ubrig, E. Giannini, and A. F. Morpurgo, Nat. Commun. **6**, 8892 (2015).
[36] X. H. Niu, D. F. Xu, Y. H. Bai, Q. Song, X. P. Shen, B. P. Xie, Z. Sun, Y. B. Huang, D. C. Peets, and D. L. Feng, Phys. Rev. B **94**, 165163 (2016).

[37] Y. Wu, T. Kong, L.-L. Wang, D. D. Johnson, D. Mou, L. Huang, B. Schrunk, S. L. Bud'ko, P. C. Canfield, and A. Kaminski, Phys. Rev. B **94**, 081108(R) (2016).

[38] J. Nayak, S.-C. Wu, N. Kumar, C. Shekhar, S. Singh, J. Fink, E. E. D. Rienks, G. H. Fecher, S. S. P. Parkin, B. Yan, and C. Felser, Nat. Commun. **8**, 13942 (2017).

[39] Y. Wu, L.-L. Wang, E. Mun, D. D. Johnson, D. Mou, L. Huang, Y. Lee, S. L. Bud'ko, P. C. Canfield, and A. Kaminski, Nat. Phys. **12**, 667 (2016).

[40] J. Hu, Z. Tang, J. Liu, X. Liu, Y. Zhu, D. Graf, K. Myhro, S. Tran, C. N. Lau, J. Wei, and Z. Mao, Phys. Rev. Lett. **117**, 016602 (2016).

[41] A. B. Pippard, *Magnetoresistance in Metals* (Cambridge University Press, Cambridge, 1989).

[42] C.-L. Zhang, Z. Yuan, Q. D. Jiang, B. Tong, C. Zhang, X. C. Xie, and S. Jia, Phys. Rev. B **95**, 085202 (2017).

[43] R. A. Smith, *Semiconductors* (Cambridge University Press, Cambridge, 1978).

[44] K. Wang, D. Graf, H. Lei, S. W. Tozer, and C. Petrovic, Phys. Rev. B **84**, 220401(R) (2011).

[45] K. Wang, D. Graf, L. Wang, H. Lei, S. W. Tozer, and C. Petrovic, Phys. Rev. B **85**, 041101(R) (2012).

[46] M. Kriener, A. Kikkawa, T. Suzuki, R. Akashi, R. Arita, Y. Tokura, and Y. Taguchi, Phys. Rev. B **91**, 075205 (2015).

[47] J. S. Kim, J. Appl. Phys. **86**, 3187 (1999).

[48] N. Kumar, Y. Sun, K. Manna, V. Süss, I. Leermakers, O. Young, T. Förster, M. Schmidt, B. Yan, U. Zeitler, C. Felser, and C. Shekhar, arXiv:1703.04527.

[49] C. Shekhar, Y. Sun, N. Kumar, M. Nicklas, K. Manna, V. Süß, O. Young, I. Leermakers, T. Förster, M. Schmidt, L. Muechler, P. Werner, W. Schnelle, U. Zeitler, B. Yan, S. S. P. Parkin, and C. Felser, arXiv:1703.03736.

[50] K. Ishizaka, M. S. Bahramy, H. Murakawa, M. Sakano, T. Shimojima, T. Sonobe, K. Koizumi, S. Shin, H. Miyahara, A. Kimura, K. Miyamoto, T. Okuda, H. Namatame, M. Taniguchi, R. Arita, N. Nagaosa, K. Kobayashi, Y. Murakami, R. Kumai, Y. Kaneko, Y. Onose, and Y. Tokura, Nat. Mater. **10**, 521 (2011).

[51] J. Jiang, F. Tang, X. C. Pan, H. M. Liu, X. H. Niu, Y. X. Wang, D. F. Xu, H. F. Yang, B. P. Xie, F. Q. Song, P. Dudin, T. K. Kim, M. Hoesch, P. K. Das, I. Vobornik, X. G. Wan, and D. L. Feng, Phys. Rev. Lett. **115**, 166601 (2015).

[52] R. Schönemann, N. Aryal, Q. Zhou, Y.-C. Chiu, K.-W. Chen, T. J. Martin, G. T. McCandless, J. Y. Chan, E. Manousakis, and L. Balicas, Phys. Rev. B **96**, 121108 (2017).